# Climate-Forced Variability of Ocean Hypoxia

Curtis Deutsch, *et al.*

*Science* **333**, 336 (2011);
DOI: 10.1126/science.1202422

*This copy is for your personal, non-commercial use only.*

**If you wish to distribute this article to others**, you can order high-quality copies for your colleagues, clients, or customers by clicking here.

**Permission to republish or repurpose articles or portions of articles** can be obtained by following the guidelines here.

***The following resources related to this article are available online at www.sciencemag.org (this infomation is current as of July 14, 2011 ):***

**Updated information and services,** including high-resolution figures, can be found in the online version of this article at:
http://www.sciencemag.org/content/333/6040/336.full.html

**Supporting Online Material** can be found at:
http://www.sciencemag.org/content/suppl/2011/06/08/science.1202422.DC1.html

This article **cites 25 articles**, 4 of which can be accessed free:
http://www.sciencemag.org/content/333/6040/336.full.html#ref-list-1

This article appears in the following **subject collections:**
Oceanography
http://www.sciencemag.org/cgi/collection/oceans

*Science* (print ISSN 0036-8075; online ISSN 1095-9203) is published weekly, except the last week in December, by the American Association for the Advancement of Science, 1200 New York Avenue NW, Washington, DC 20005. Copyright 2011 by the American Association for the Advancement of Science; all rights reserved. The title *Science* is a registered trademark of AAAS.

# Climate-Forced Variability of Ocean Hypoxia

Curtis Deutsch,[1]* Holger Brix,[1] Taka Ito,[2]† Hartmut Frenzel,[1] LuAnne Thompson[3]

**Oxygen ($O_2$) is a critical constraint on marine ecosystems. As oceanic $O_2$ falls to hypoxic concentrations, habitability for aerobic organisms decreases rapidly. We show that the spatial extent of hypoxia is highly sensitive to small changes in the ocean's $O_2$ content, with maximum responses at suboxic concentrations where anaerobic metabolisms predominate. In model-based reconstructions of historical oxygen changes, the world's largest suboxic zone, in the Pacific Ocean, varies in size by a factor of 2. This is attributable to climate-driven changes in the depth of the tropical and subtropical thermocline that have multiplicative effects on respiration rates in low-$O_2$ water. The same mechanism yields even larger fluctuations in the rate of nitrogen removal by denitrification, creating a link between decadal climate oscillations and the nutrient limitation of marine photosynthesis.**

Numerous biological and physiological processes have $O_2$ thresholds that restrict the activity and habitat of marine organisms, from microbes to macrofauna. Concentrations of dissolved $O_2$ below ~60 μM, termed hypoxic, are lethal for more than 50% of marine benthic animals; this proportion increases to more than 90% when $O_2$ falls below ~10 μM (*1*). Microbial communities also undergo a marked shift under low oxygen conditions. At suboxic concentrations ($O_2 < 5$ μM), anaerobic processes such as denitrification and anaerobic ammonium oxidation become dominant metabolic pathways (*2*) that account for half of the global fixed nitrogen removal from the ocean, yielding widespread nitrogen limitation of photosynthesis (*3*).

As the ocean continues to absorb heat from anthropogenic climate warming, its $O_2$ content is expected to decline because surface heating reduces gas solubility and inhibits the mixing of $O_2$-rich surface water into the deeper ocean, where $O_2$ is continually removed by microbial respiration (*4*, *5*). Historical observations suggest that a loss of $O_2$ may already be under way (*6*, *7*); however, the paucity of data and the presence of strong decadal oscillations preclude the detection or attribution of global trends (*8*–*11*). Few long-term observations are available in hypoxic regions (*12*–*14*), and none in suboxic zones (*10*). However, these are the regions where deoxygenation is likely to have the greatest biological and biogeochemical consequences, because $O_2$ levels are already at or near biological thresholds.

The potential sensitivity of hypoxic regions to changes in climate can be illustrated by considering the volume of ocean, $V_{O_2}$, in which $O_2$ falls below a threshold concentration, $O_2^{crit}$ (Fig. 1A). In the contemporary ocean, hypoxic conditions ($O_2 < 60$ μM) occupy ~5% of the ocean volume ($7.6 \times 10^{16}$ m$^3$) but are pervasive in the eastern Pacific Ocean and northern Indian Ocean at thermocline depths (100 to 1000 m) where warm surface water transitions to the cold abyss and most respiration occurs. The spatial extent of low-$O_2$ waters declines rapidly as $O_2^{crit}$ decreases, so that suboxic conditions are found in ~0.1% of the ocean ($4.5 \times 10^{14}$ m$^3$), 95% of it in the eastern tropical North Pacific (*15*).

A change in $V_{O_2}$ at any value of $O_2^{crit}$ represents a loss or gain of habitat for any species or process constrained by that threshold. A rough estimate of the sensitivity of $V_{O_2}$ to changes in ocean oxygenation can be derived from the time-mean distribution of $O_2$. For a large-scale oxygen anomaly of magnitude $\Delta O_2$, the effect on $V_{O_2}$ can be estimated directly from climatological observations as $\Delta V_{O_2} = V_{O_2 + ½\Delta O_2} - V_{O_2 - ½\Delta O_2}$ (Fig. 1B). For example, a decline in mean $O_2$ solubility of ~5 μM attending a hypothetical warming of 1°C throughout the upper ocean would expand the reach of hypoxic conditions by 10% while suboxic zones would nearly triple in volume. Relative to their present size, suboxic zones ($O_2 < 5$ μM) are particularly sensitive: A doubling in size requires only a 1% drop (~2 μM) in mean $O_2$ of the upper ocean (Fig. 1B). The rapid decline in ocean volume as $O_2^{crit}$ decreases is a characteristic of the mean oceanic $O_2$ distribution that makes the extent of low-$O_2$ waters intrinsically vulnerable to even modest physical perturbations. Of course, the actual variability of hypoxic zones will depend

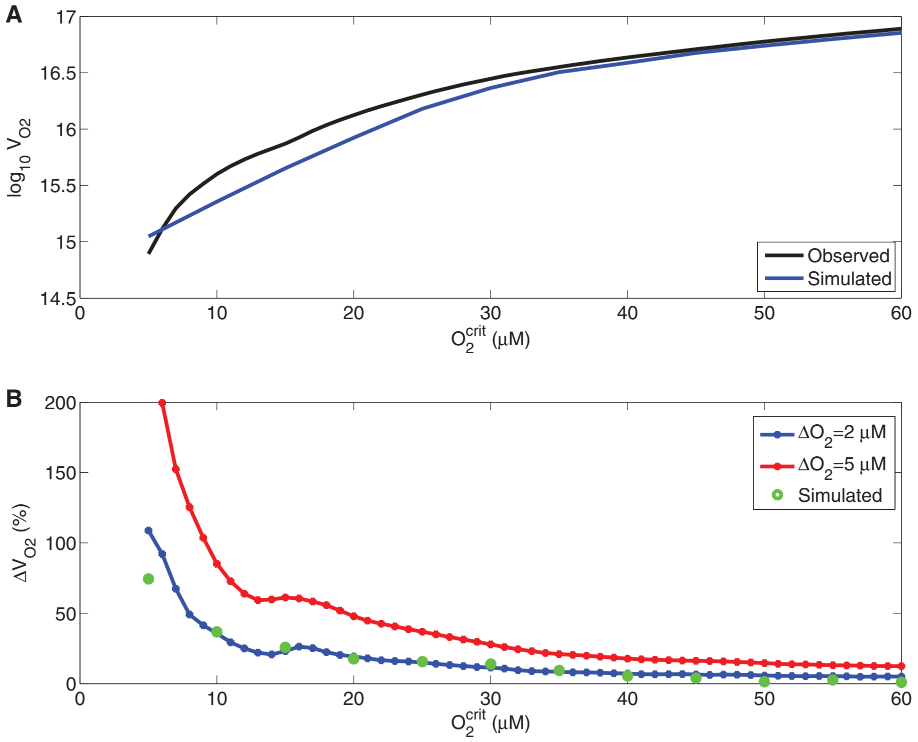

**Fig. 1.** (**A** and **B**) Global ocean hypoxic volume versus $O_2$ threshold for long-term mean conditions (A) and its amplitude of variation over time (B). Hypoxic volumes, $V_{O_2}$, of the ocean are computed as the annual mean volume of water in which $[O_2] < [O_2^{crit}]$ using climatological observations (*27*) and ocean model simulations (see supporting online material). A potential amplitude of variation is calculated from observations as $\Delta V_{O_2} = V_{O_2 + ½\Delta O_2} - V_{O_2 - ½\Delta O_2}$, where $\Delta O_2$ is a uniform hypothetical $O_2$ concentration anomaly. Values of $\Delta V_{O_2}$ are plotted relative to the time-mean value for $\Delta O_2 = 5$ μM (red line) corresponding to a 1°C temperature change, and for $\Delta O_2 = 2$ μM (blue line), the global mean standard deviation of $O_2$ simulated from 1959 to 2005. Amplitudes of $\Delta V_{O_2}$ computed directly from the model hindcast (green circles) closely follow the potential changes predicted empirically from climatological observations, confirming the intrinsic sensitivity of hypoxic waters.

---

[1] Department of Atmospheric and Oceanic Sciences, University of California, Los Angeles, CA 90095, USA. [2] Department of Atmospheric Science, Colorado State University, Fort Collins, CO 80523, USA. [3] School of Oceanography, University of Washington, Box 355351, Seattle, WA 98195, USA.

*To whom correspondence should be addressed. E-mail: cdeutsch@atmos.ucla.edu

†Present address: School of Earth and Atmospheric Sciences, Georgia Institute of Technology, Atlanta, GA 30332, USA.

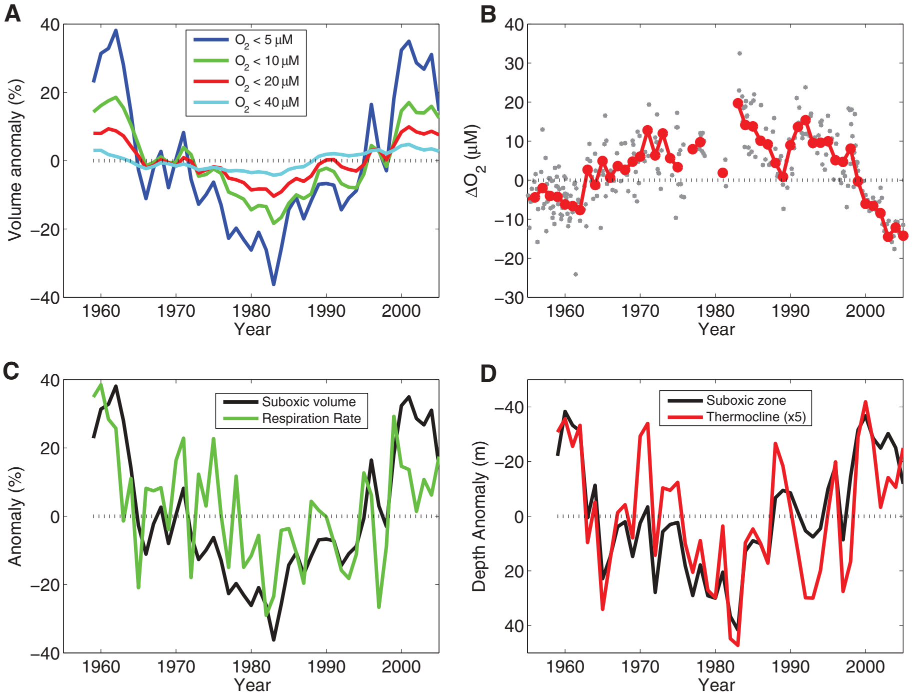

**Fig. 2.** (**A** to **D**) Time series from 1959 to 2005 of simulated changes in global hypoxic water volumes (A), observed $O_2$ anomaly off the coast of California (B), changes in respiration rate (C), and depth anomalies of the thermocline (13°C isotherm, red) and top of the suboxic zone (black) (D) in the eastern tropical Pacific Ocean, which contains 95% of the ocean's suboxic water. Observed $O_2$ anomalies are mean monthly (gray) and annual (red) values averaged over water depths of 250 to 300 m throughout the region sampled by the CalCOFI program (downloaded from www.calcofi.org). Changes in volumetric respiration rate (mol $O_2$ $m^{-3}$ $year^{-1}$) are averaged over waters surrounding the suboxic zone with $O_2 < 20$ µM and normalized to the time mean value. Depth anomalies are averaged over the region from 0° to 30°N, 140°W to the coast, and plotted with shallower depths upward. Fluctuations in the depth of the suboxic zone are larger than for the thermocline by a factor of ~5 because of the multiplicative effects of thermocline depth on export flux and respiration.

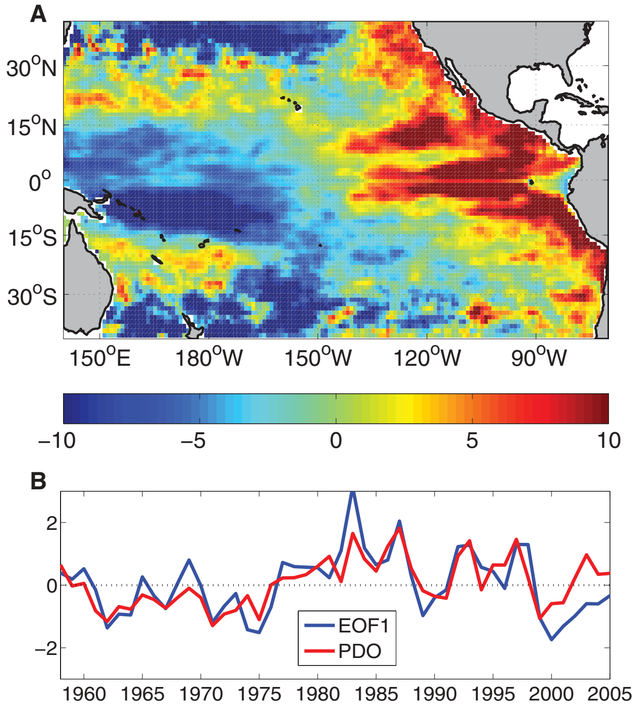

**Fig. 3.** (**A** and **B**) Leading empirical orthogonal function (EOF) of Pacific thermocline depth, based on the Simple Ocean Data Assimilation (SODA) state estimate (*18*) covering the period 1958–2007. The EOF is computed from annual mean departures from the long-term average depth (in meters) of the 13°C isotherm, which lies within the suboxic zone. The product of the spatial pattern (A) and the time series (B) gives the depth anomaly (in meters) associated with this mode at any location and time. The first mode contains 13% of the total variance of annually averaged thermocline depth equatorward of 40°. Thermocline depth throughout the upwelling regions of the eastern and equatorial Pacific Ocean varies in concert on multidecadal time scales, and is highly coherent with the Pacific Decadal Oscillation (PDO) index for North Pacific sea surface temperature variability. Negative values (blue shading) indicate shallower than average thermocline during cool phases of the PDO; positive values (red shading) indicate deeper than average thermocline during its warm phase.

not only on the magnitude of $\Delta O_2$ but also on its distribution in space and time, which may be quite complex.

To test the predicted sensitivity of low-$O_2$ regions and diagnose the underlying mechanisms, we reconstructed changes in the global $O_2$ distribution over the past half-century with the use of numerical simulations of the oxygen cycle in an ocean general circulation model (GCM) (*16*) that is forced by reanalyzed atmospheric winds and buoyancy fluxes at the sea surface from 1959 to 2005 (see supporting online material). The model simulations reproduce the observed time-averaged volumetric census of $O_2$ and its spatial distribution (Fig. 1A and figs. S1 to S3). The annual mean fluctuations of $O_2$ have a standard deviation of ~2 µM when averaged throughout the ocean. The amplitude of variations in the spatial extent of low-$O_2$ conditions (Fig. 1B, green circles) increases from ~10% at $O_2^{crit}$ = 40 µM to nearly 100% at suboxic levels. Although these simulated fluctuations in the scale of hypoxia arise from a complex spatial and temporal pattern of $O_2$ variability, they nonetheless follow the rough empirical estimate, thus confirming the simple prediction that low-$O_2$ waters are naturally prone to large expansions and contractions.

Changes in the global volume of low-$O_2$ water are coherent in time across the range of hypoxic thresholds (Fig. 2A) and are dominated by the Pacific Ocean, where most of these waters reside. Hypoxic volume fluctuations can occur on an interannual time scale, but these are strongly modulated by a slower apparent oscillation over decades. Although the historical database for oceanic $O_2$ concentrations is not adequate to directly assess temporal changes in the volume of hypoxic water, the longest existing $O_2$ time series in the world—from the California Cooperative Oceanic Fisheries Investigation (CalCOFI)—lies within the hypoxic zone off the coast of southern California (*13*, *14*). The oxygen anomalies observed in this region reveal a multidecadal oscillation that is consistent with model simulations (Fig. 2B). The correspondence between the simulated tropical Pacific suboxic zone and observed $O_2$ concentration anomalies in the hypoxic region to its north implies a mode of biogeochemical variability that is synchronized by large-scale physical forcing.

The proximate cause of changes in the volume of the suboxic zone is the rate of organic matter respiration in surrounding low-$O_2$ waters (Fig. 2C). An increase in volumetric respiration rate produces a rapid increase in the volume of suboxic water, whereas a reduction in respiration rate in the presence of continued physical supply of $O_2$ by ocean circulation and mixing causes suboxic boundaries to contract. The physical transport of $O_2$ into the suboxic zones by modeled ocean circulation (fig. S4) is much less variable on decadal time scales than is the respiration rate, and is not correlated with changes in suboxic extent. However, changes in the respiration rate are ultimately driven by physical perturbations.

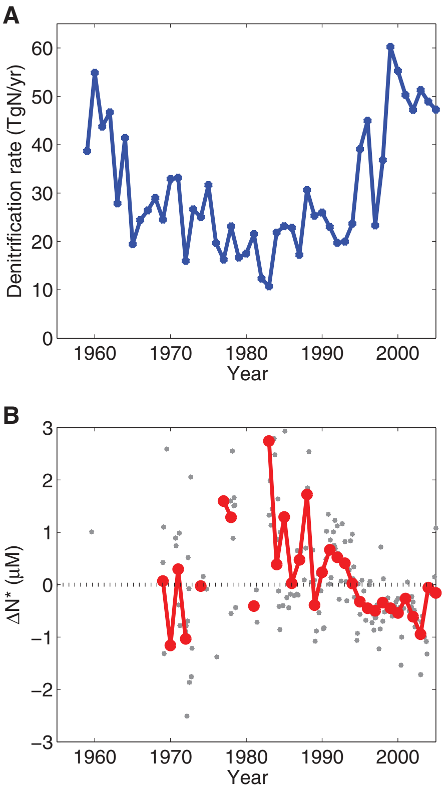

**Fig. 4.** (**A** and **B**) Time series of integrated denitrification rate (Tg N/year) in the suboxic zone of the eastern tropical North Pacific (A) and observed anomalies in nitrate relative to phosphate ($N^* = [NO_3^-] - 16[PO_4^{3-}]$) along the California margin (B). Denitrification rates are calculated from the modeled remineralization rate of organic matter in suboxic waters, assuming a stoichiometry of 104N:1P (*20*). N* anomalies are spatially averaged deviations from the long-term mean at 250 to 300 m throughout the region sampled by the CalCOFI program. Spatially averaged values of N* are always negative, indicating a deficit of nitrate and thus persistent nitrogen limitation, but the deficit is smaller than normal ($\Delta N^* > 0$) during periods of weakest simulated denitrification.

The depth of the tropical and subtropical thermocline is the key modulator of suboxic volume (Fig. 2D) for two related reasons. (The 13°C isotherm, which lies near the top of the North Pacific suboxic zone, is hereafter taken as an index of thermocline depth.) First, a shallow thermocline enhances the flux of nutrients into the sunlit surface layer, resulting in greater biological productivity and a larger flux of organic matter that sinks to depth, a phenomenon supported by satellite chlorophyll data (*17*). Second, because the low-$O_2$ waters lie within the thermocline, a shoaling of these waters simultaneously increases the fraction of the exported particles that are respired under already low-$O_2$ conditions, causing respiration in the neighborhood of the suboxic zone to vary more than twice as much as export production (fig. S5). The top of the suboxic zone plunges and shoals in concert with the thermocline, but its vertical displacements are amplified by a factor of ~5 because of the combined effect of thermocline depth on both productivity and fractional respiration.

Thermocline depth fluctuations in the hypoxic zones of the eastern tropical Pacific are part of a basin-scale pattern of thermocline variability that is closely connected to Pacific climate. Changes in upwelling strength and thermocline depth associated with El Niño and the Southern Oscillation (ENSO) also affect model simulated productivity, respiration, and lateral transport of $O_2$ (figs. S4 and S5). However, these oscillations are rapid relative to the residence time of waters in the suboxic zone, which is ~10 years in the GCM. The effect of ENSO forcing on large-scale $O_2$ anomalies is therefore greatly attenuated (*11*).

The principal spatial pattern of decadal variations in thermocline (13°C isotherm) depth across the entire Pacific Ocean includes a coherent rising and falling of the thermocline throughout the eastern Pacific, both in our model simulations (fig. S6) and in models that assimilate hydrographic data (*18*) (Fig. 3). This pattern of thermocline variation is highly correlated ($r^2 = 0.67$, $P << 0.01$) with the Pacific Decadal Oscillation (PDO), an index of North Pacific sea surface temperature variation (*19*), and thus represents the thermocline manifestation of that well-known mode of surface climate. Variations in thermocline depth in the vicinity of the tropical Pacific suboxic zones are governed by a complex mixture of local wind forcing and basin-scale circulation, but the PDO alone explains 24% of the variability in Pacific suboxic zone volume ($P < 0.05$).

The expansion and contraction of hypoxic zones on interannual and decadal time scales has important implications for marine ecosystems, especially for microbial nitrogen transformations that are confined to suboxic waters. Assuming a constant stoichiometric relationship between the remineralization of $PO_4^{3-}$ and the rate of denitrification in suboxic waters of 104N:1P (*20*), our model predicts that the annual rate of denitrification in the eastern tropical North Pacific has varied by a factor of 4 during the past 50 years (Fig. 4A). Roughly half of this variation comes from the fluctuating volume of suboxia; the other half stems from the high rates of respiration that produce both larger suboxic zones and a higher volumetric rate of denitrification within them. The mean nitrate loss rates predicted here (30 Tg N/year in the North Pacific) are similar to observational estimates, whose large uncertainty may in part reflect the actual variability of this process (*21*).

The denitrified waters of the North Pacific suboxic zone are exported to the wider Pacific basin (*22*, *23*), yielding widespread nitrogen limitation. Low-frequency variability in the intensity of denitrification should therefore be observable in geochemical tracers of this process well beyond its locus. Indeed, the surplus or deficit of nitrate relative to phosphate, indicated by the quantity N* ($N^* = [NO_3^-] - 16[PO_4^{3-}]$), also exhibits a multidecadal oscillation in the CalCOFI region that is consistent in phase and sign with model-reconstructed denitrification rates (Fig. 4B). The amplitude of this fluctuation, ~3 μM, represents a substantial perturbation to the nitrate reservoir, and suggests that climate-driven thermocline depth variations may modulate the strength of nitrogen limitation of marine photosynthesis across much of the low-nutrient Pacific Ocean.

The predictable effect of warming on the solubility of $O_2$ in the surface ocean will promote expansion of hypoxic water masses in the ocean interior, especially for waters already at the lowest $O_2$ levels. However, the sensitivity of hypoxic zones to variations in the depth of the thermocline introduces a mechanism for counteracting this expansion. If continued warming leads to a deeper thermocline in the tropics, this will diminish the oxidative demand in low-$O_2$ thermocline waters, potentially leading to a contraction of suboxic conditions. Geological records from shallow bottom waters along the North American margin suggest that the expansion of suboxic zones since the Last Glacial Maximum was not a monotonic process, but was instead characterized by transient expansions and overshoots (*24*); this in turn suggests that the adjustment of the $O_2$ distribution to climate warming involves multiple mechanisms and time scales. Given the relatively short and sparse instrumental records, high-resolution sedimentary reconstruction of ocean oxygenation and its effect on denitrification (*25*, *26*) provide an important avenue for evaluating the past and future impacts of anthropogenic warming on low-$O_2$ regions.

### References and Notes

1. R. Vaquer-Sunyer, C. M. Duarte, *Proc. Natl. Acad. Sci. U.S.A.* **105**, 15452 (2008).
2. B. B. Ward *et al.*, *Nature* **461**, 78 (2009).
3. L. A. Codispoti, in *Productivity of the Ocean: Past and Present*, W. H. Berger, V. S. Smetacek, G. Wefer, Eds. (Wiley-Interscience, New York, 1989), pp. 377–394.
4. R. F. Keeling, H. E. Garcia, *Proc. Natl. Acad. Sci. U.S.A.* **99**, 7848 (2002).
5. L. Bopp, C. Le Quéré, M. Heimann, A. C. Manning, P. Monfray, *Global Biogeochem. Cycles* **16**, 1022 (2002).
6. F. A. Whitney, H. J. Freeland, M. Robert, *Prog. Oceanogr.* **75**, 179 (2007).
7. F. Chan *et al.*, *Science* **319**, 920 (2008).
8. S. Mecking *et al.*, *Global Biogeochem. Cycles* **22**, GB3015 (2008).
9. S. Emerson, Y. W. Watanabe, T. Ono, S. Mecking, *J. Oceanogr.* **60**, 139 (2004).
10. R. F. Keeling, A. Körtzinger, N. Gruber, *Annu. Rev. Mar. Sci.* **2**, 199 (2009).
11. T. Ito, C. Deutsch, *Geophys. Res. Lett.* **37**, L03601 (2010).
12. L. Stramma, S. Schmidtko, L. A. Levin, G. C. Johnson, *Deep Sea Res. I* **57**, 587 (2010).
13. S. McClatchie, R. Goericke, R. Cosgrove, G. Auad, R. Vetter, *Geophys. Res. Lett.* **37**, L19602 (2010).
14. S. J. Bograd *et al.*, *Geophys. Res. Lett.* **35**, L12607 (2008).
15. J. Karstensen, L. Stramma, M. Visbeck, *Prog. Oceanogr.* **77**, 331 (2008).
16. R. Hallberg, A. Gnanadesikan, *J. Phys. Oceanogr.* **36**, 2232 (2006).
17. E. Martinez, D. Antoine, F. D'Ortenzio, B. Gentili, *Science* **326**, 1253 (2009).
18. J. Carton, B. Giese, *Mon. Weather Rev.* **136**, 2999 (2008).
19. N. J. Mantua, S. R. Hare, Y. Zhang, J. M. Wallace, R. C. Francis, *Bull. Am. Meteorol. Soc.* **78**, 1069 (1997).

20. L. A. Anderson, J. L. Sarmiento, *Global Biogeochem. Cycles* **8**, 65 (1994).
21. L. A. Codispoti *et al.*, *Sci. Mar.* **65** (suppl. 2), 85 (2001).
22. C. Deutsch, N. Gruber, R. M. Key, J. L. Sarmiento, A. Ganachaud, *Global Biogeochem. Cycles* **15**, 483 (2001).
23. C. G. Castro, F. P. Chavez, C. A. Collins, *Global Biogeochem. Cycles* **15**, 819 (2001).
24. A. van Geen *et al.*, *Paleoceanography* **18**, 1098 (2003).
25. R. S. Ganeshram, T. F. Pedersen, S. E. Calvert, J. W. Murray, *Nature* **376**, 755 (1995).
26. M. A. Altabet, R. Francois, D. W. Murray, W. L. Prell, *Nature* **373**, 506 (1995).
27. H. Garcia, R. A. Locarnini, T. P. Boyer, J. I. Antonov, in *NOAA Atlas NESDros. Inf. Serv.* (U.S. Government Printing Office, Washington, DC, 2006), vol. 63.

**Acknowledgments:** Supported by a grant from the Gordon and Betty Moore Foundation (C.D.) and NSF grants OCE-0851483 (C.D.) and OCE-0851497 (T.I.).

**Supporting Online Material**
www.sciencemag.org/cgi/content/full/science.1202422/DC1
Materials and Methods
Figs. S1 to S7
References

3 January 2011; accepted 27 May 2011
Published online 9 June 2011;
10.1126/science.1202422

---

# Chirality in Planar Cell Shape Contributes to Left-Right Asymmetric Epithelial Morphogenesis

Kiichiro Taniguchi,[1]* Reo Maeda,[1]* Tadashi Ando,[1] Takashi Okumura,[1] Naotaka Nakazawa,[1] Ryo Hatori,[1] Mitsutoshi Nakamura,[1] Shunya Hozumi,[1] Hiroo Fujiwara,[1] Kenji Matsuno[1,2]†

Some organs in animals display left-right (LR) asymmetry. To better understand LR asymmetric morphogenesis in *Drosophila*, we studied LR directional rotation of the hindgut epithelial tube. Hindgut epithelial cells adopt a LR asymmetric (chiral) cell shape within their plane, and we refer to this cell behavior as planar cell-shape chirality (PCC). *Drosophila* E-cadherin (*D*E-Cad) is distributed to cell boundaries with LR asymmetry, which is responsible for the PCC formation. Myosin ID switches the LR polarity found in PCC and in *D*E-Cad distribution, which coincides with the direction of rotation. An in silico simulation showed that PCC is sufficient to induce the directional rotation of this tissue. Thus, the intrinsic chirality of epithelial cells in vivo is an underlying mechanism for LR asymmetric tissue morphogenesis.

Directional left-right (LR) asymmetry is widely found in animals, such as in the position and structure of the heart, spleen, gut, and lung in vertebrates (*1*). The mechanisms of LR axis formation are well understood in some vertebrates (*1*), and the cellular basis for LR symmetry breaking, including cell polarities, is beginning to be elucidated (*2*, *3*). *Drosophila* shows a directional LR asymmetry of certain organs, including the embryonic hindgut (*4*, *5*). Although some unique features of *Drosophila* laterality development have been revealed, such as the involvement of myosin ID (MyoID) (*4*, *5*), the detailed mechanisms of its LR asymmetric development remain largely unknown.

The *Drosophila* embryonic hindgut begins as a symmetric midline structure that curves ventrally at stage 12 (Fig. 1A and fig. S1A). It subsequently makes a 90° left-handed rotation, forming a rightward curving structure by stage 13 (Fig. 1A) (*6*). The hindgut epithelium, but not the overlying visceral muscles, is responsible for this rotation, which is not accompanied by cell proliferation or cell death (*6*). Therefore, we speculated that the hindgut epithelial cells themselves might have LR polarity, which could contribute to the rotation.

To analyze LR polarity in the hindgut epithelial cells, we examined the locations of the centrosomes, which reflect cell polarity in other systems (*7*, *8*). We calculated each cell's centroid with respect to its boundaries and plotted the relative position of the centrosome, labeled with green fluorescent protein (GFP)–centrosomin (Fig. 1, B and C). In wild-type animals, the relative position of the centrosome was significantly biased to the right-posterior region (Fig. 1, D and E). These results suggest that hindgut epithelial cells adopt a LR polarity within their plane before the hindgut rotates.

We speculated that this LR polarity would be reflected in the cell shape and participate directly in the left-handed rotation. To address this, we measured the angle between apical cell boundaries and the antero-posterior (AP) axis of the hindgut epithelial tube before rotation (late-stage 12) ($x$° in Fig. 2A). These apical cell boundaries corresponds to the zonula adherens (ZA). Cell-boundary angles of −90° to 0° to the AP axis were more frequent than those of 0° to 90°, indicating that hindgut epithelial cells have a LR-biased planar cell shape (Fig. 2B). We designated this LR bias as planar cell-shape chirality (PCC), because the mirror image of the cell's planar shape does not overlap with its original cell shape.

We previously demonstrated that the hindgut rotates right-handedly in embryos homozygous for *Myo31DF*, which encodes MyoID (*4*). In $Myo31DF^{L152}$ homozygotes, the distribution of angle $x$° was reversed from that of wild type, although the LR bias became less prominent (compare Fig. 2, B and C). The reversed PCC in $Myo31DF^{L152}$ was rescued by the overexpression of $Myo31DF^{GFP}$ (Fig. 2D). Rho family guanosine triphosphatases, including Rho1 and Rac1, regulate the organization of the actin cytoskeleton

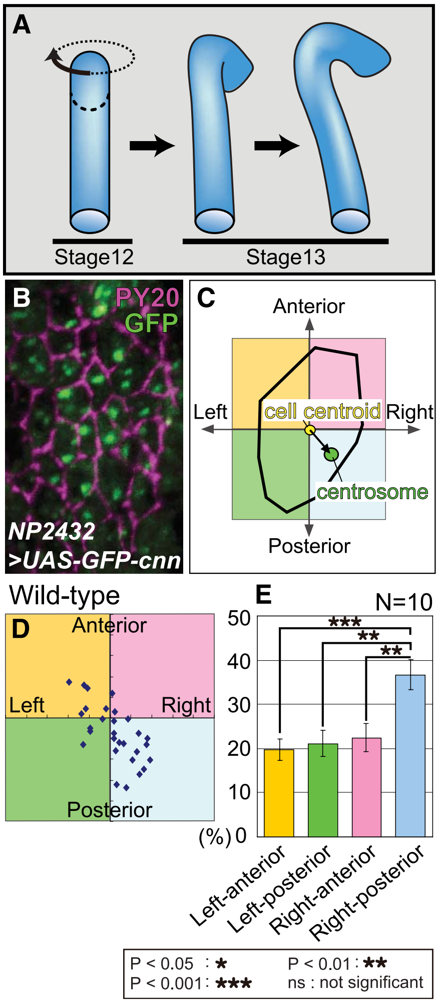

**Fig. 1.** Polarization of centrosome positions in hindgut epithelial cells. (**A**) Schematic drawing of the left-handed rotation of the wild-type hindgut. (**B**) Centrosomes (green) visualized by *UASp-GFP-cnn* expression driven by *NP2432*. Cell boundaries were detected by antibody against PY20 (anti-PY20) (magenta). (**C**) Diagram representing the position of a centrosome relative to the cell centroid in two-dimensional coordinates (anterior-posterior and left-right). (**D**) Representative result showing the positions of centrosomes (blue dots) in a wild-type hindgut. (**E**) Percentages of centrosomes plotted on the four areas of (D). Bars show standard errors among the means of 10 embryos.

---

[1] Department of Biological Science and Technology, Tokyo University of Science, 2641 Yamazaki, Noda, Chiba 278-8510, Japan. [2] Research Institute for Science and Technology, Tokyo University of Science, 2641 Yamazaki, Noda, Chiba 278-8510, Japan.

*These authors contributed equally to this work.

†To whom correspondence should be addressed. E-mail: matsuno@rs.noda.tus.ac.jp